Case Studies in Construction Materials 17 (2022) e01397

Contents lists available at ScienceDirect

Case Studies in Construction Materials

journal homepage: www.elsevier.com/locate/cscm

Short communication

Effects of basalt powder and silica fume on ultra-high-strength cementitious matrix: A comparative study

Manlin Shen [a], Lixiao Zhou [a], Zuyong Chen [a], Yinong Shen [a,c,*], Botao Huang [b,**], Jianfu Lv [c]

[a] Zhejiang Huian Engineering Quality Inspection Co., Ltd., Hangzhou 310000, China
[b] Department of Civil and Environmental Engineering, The Hong Kong Polytechnic University, Hong Kong, China
[c] College of Aerospace and Civil Engineering, Harbin Engineering University, Harbin 150001, China

ARTICLE INFO

Keywords:
Cementitious matrix
Basalt powder
Microstructure
Hydration
Silica fume
Ultra-High-Performance Concrete (UHPC)

ABSTRACT

Understanding the effects of basalt powder on the microstructures and hydration products of ultra-high-strength cementitious matrices (UHSCMs) can contribute to the application of basalt powder in ultra-high-performance concrete. This study assesses the effects of basalt powder and silica fume on cementitious matrices by strength examination, microstructure analysis, and material characterization. The results prove the feasibility of adding basalt powder to UHSCMs. Both basalt powder and silica fume can function as reactive additives for cementitious matrices and improve silicate polymerization in calcium silicate hydrate (C-S-H) gels. The calcium-enrichment of the cementitious matrices containing basalt powder leads to the decalcification of the C-S-H structure, the refinement of the pore structure, and the decrease in the strength of UHSCMs. Moreover, a high-temperature curing procedure can alleviate the above adverse effects of basalt powder on the strength of cementitious matrices. The findings of this study are useful for improving the sustainability of concrete materials with high and ultra-high performance.

1. Introduction

Ultra-high-strength cementitious matrices (UHSCMs) are widely used in construction [1–3]. Their low water-to-binder ratios and dense pore structures ensure their high/ultra-high strength [4–6]. However, due to the significant CO_2 emissions from cement production and exploitation of natural resources, developing eco-friendly alternative binders and aggregates for the concrete industry has been emphasized [7–11]. In this context, basalt powder will be used as a replacement for cement and utilized in UHSCMs. As a by-product and solid waste of basalt rock crushing, basalt powder causes environmental pollution and health risks in basalt quarries [12]. Thus, plenty of basalt powder is stacked for landfilling. To further utilize this solid waste, some studies evaluated the use of basalt powder as a replacement of fine aggregate to enhance concrete properties [5,13–16]. However, due to its fine grain structure and hydration activity [12], it is feasible to recycle basalt powder as a reactive admixture in cement-based binders [17].

The transportation of silica fume is inconvenient in parts of western China due to the lack of iron plants and good infrastructure. Conversely, basalt rock is widespread in those places [18], and infrastructure construction produces other basalt waste. Thus, recycling

* Corresponding author at: Zhejiang Huian Engineering Quality Inspection Co., Ltd., Hangzhou 310000, China.
** Corresponding author.
E-mail addresses: hzhuian001@163.com (M. Shen), hanxue1980@126.com (L. Zhou), chenzuyong8804@163.com (Z. Chen), shenyinong@zju.edu.cn (Y. Shen), botaohuang@zju.edu.cn (B. Huang), lvjianfu@hrbeu.edu.cn (J. Lv).

https://doi.org/10.1016/j.cscm.2022.e01397
Received 21 June 2022; Received in revised form 22 July 2022; Accepted 11 August 2022
Available online 12 August 2022

basalt waste provides enormous economic benefits.

However, the hydration process of basalt powder in cement is unclear, and how basalt powder performs in cement-based materials should be investigated. Basalt powder has successfully been used in self-compacting concrete [19,20] and ultra-high-performance concrete [18]. Basalt powder has pozzolanic activity due to its high content of SiO_2 and Al_2O_3 [13,21]. It also retards the hydration heat evolution and the development of the early-age strength of cement pastes [21]. Compared with silica fume, using basalt powder in UHSCMs is rare to see.

In the last decade, silica fume has been used as a cement replacement and in high-strength cement mortars [22,23]. Indeed, a suitable combination of silica fume and cement can enhance the mechanical properties of UHSCMs and refine their microstructure [23]. Thus, both silica fume and basalt powder are eco-friendly supplementary cementitious materials. UHSCMs have a low cement hydration degree because of their low water-to-binder ratio, and it has been verified that silica fume can enhance the hydration degree of UHSCMs [24]. Some studies have reported the low pozzolanic activity of basalt powder in cement-based materials [13,18,21]. However, the investigation into the effects of basalt powder on the microstructure and hydration products of UHSCMs is still inadequate, which is associated with the durability and mechanical properties of UHSCMs containing basalt powder, further influencing the application of basalt powder.

Therefore, the main objectives of this study are to evaluate the feasibility of adding basalt powder into UHSCMs, compare the cementitious matrix containing silica fume with that containing basalt powder, and explore the effects of basalt powder on the microstructures and hydration products of UHSCMs. To this end, the strength of UHSCMs containing basalt powder and silica fume is analyzed under different curing conditions. Mercury intrusion porosimetry (MIP) and scanning electron microscopy (SEM) are also utilized to observe the microstructure of the prepared UHSCMs. Furthermore, X-ray diffraction (XRD), Fourier transform infrared (FTIR) spectroscopy, X-ray photoelectron spectroscopy (XPS), and nuclear magnetic resonance (NMR) are adopted to characterize the main hydration products. This study can also expand the application of basalt powder and provide economic and environmental benefits.

2. Experimental procedures

2.1. Mix proportion and sample preparation

Ordinary Portland cement, silica fume, and basalt powder were used as the binder materials. The raw materials are presented in Fig. 1a and b. Table 1 lists the physicochemical properties of the Portland cement, silica fume, and basalt powder determined by X-ray

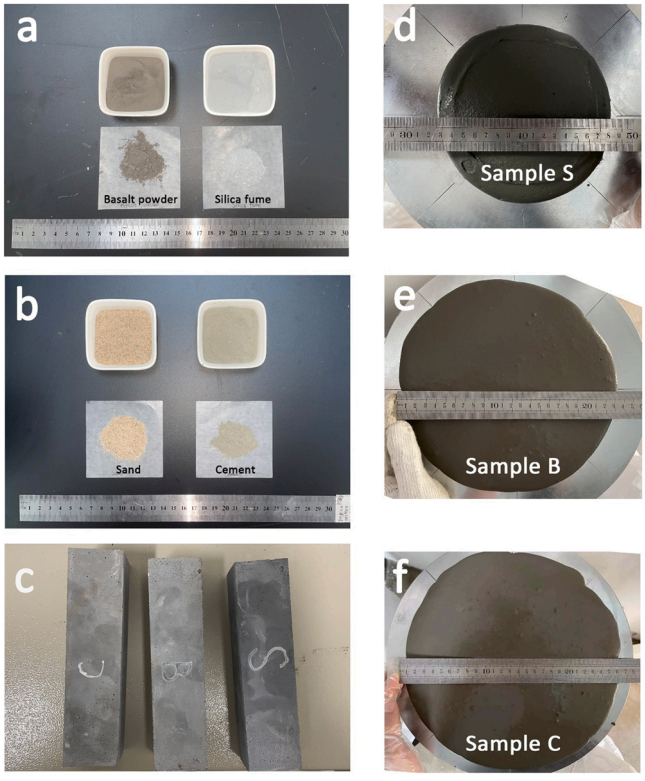

Fig. 1. Photos of (a) basalt powder and silica fume, (b) sand and cement, (c) demolded specimens, and slump-flow tests of sample S (d), sample B (e) and sample C (f).

fluorescence (XRF). This work also uses ultrafine silica sand with an average diameter of 0.1 mm and a density of 2.62 g/cm^3. Table 2 presents the mix proportion of all samples. Based on a previous study [25], the dosage of silica fume and basalt powder is fixed at 20% by the total mass of the binder. A polycarboxylate-based superplasticizer (SP) with water-reducing efficiency greater than 30% is also used. Fig. 2 depicts the particle size distribution of the raw materials determined by a laser particle analyzer (LPA).

All raw materials were premixed in a mixer at a low mixing speed of 120 ± 5 rpm for about 1 min in a dry state. Then, the superplasticizer and water were added to the mixer and mixed at a low speed for 60 s and a high speed of 270 ± 10 rpm for 2 min. The slump-flow tests were conducted on fresh mortar before casting (Figs. 1d, 1e, and 1 f) [26]. Nine specimens with the dimensions 40 mm × 40 mm × 160 mm were cast in steel molds for each mixture. The molds were covered with plastic foil before demolding, and the specimens were demolded after 24 h (Fig. 1c). Two curing procedures were utilized for strength tests:

(1) The room-temperature curing procedure: six specimens were cured in a curing chamber at a temperature of 20 ± 2 °C and relative humidity of 95 ± 5% for 28 days;
(2) The high-temperature curing procedure: three specimens were cured in a water bath box at a temperature of 90 °C for 6 h.

2.2. Testing procedures

The compressive strength and flexural strength of the mortars cured under different conditions were tested according to the National Standard of China, GB/T17671–1999 [27]. Three-point bending testing was first performed to obtain the flexural strength of the mortars, and then the compressive strength of the mortars was tested using the broken specimens. The means of three flexural strength values and six compressive strength values were reported.

MIP was utilized to study the pore structure of the UHSCMs cured by the room-temperature curing procedure. The MIP tests could measure the pore diameter range of 3 nm to 350 μm. To further analyze the pore structure of the UHSCMs, the pore distribution was divided into four size ranges: gel pores (3.0–4.5 nm), mesopores (4.5–50.0 nm), medium capillary pores (50–100 nm), and large capillary pores (100–1000 nm) [28].

Scanning electron microscopy–energy-dispersive X-ray spectrometry (SEM–EDXS) was employed to observe the microstructure of the UHSCMs and determine the distribution of elements Mg, Ca, Si, and Fe. For backscattered scanning electron microscopy (BSEM) observation, crushed sample B was further impregnated with low viscosity epoxy resin and polished down to 5 μm.

XPS with an Al-Kα X-ray source was operated at 72 W (12 kV and 6 mA). The area for the XPS analysis was 3 mm in diameter. The system was operated with a 50 eV pass energy, and Advantage software extracted the data from the spectra via peak fitting. The specimens for the XPS were etched to avoid the influence of carbonation. The spectra of the XPS were also corrected using the adventitious carbon peak at 284.8 eV.

FTIR was used in a wavenumber range of 4000–600 cm^{-1}. Clean attenuated total reflectance (ATR) diamond crystal recorded the background spectra. The software Origin 2020 was used to analyze the spectra.

XRD with Cu-Kα radiation and a continuous scanning pattern at a 2θ angle ranging from 10° to 80° analyzed all cement mortars cured using the room-temperature curing procedure.

Moreover, ^{29}Si nuclear magnetic resonance was used at a repeating time of 4.0 s and a contact time of 6.5 μs using a 4 mm probe. There were Q^n peaks in the NMR curves, where Q indicated an SiO_4 tetrahedron unit, and n represented its connectivity degree [29].

3. Results and discussion

3.1. Compressive and flexural strengths

The partial substitution of basalt powder for cement maintains the high-strength performance of the cementitious matrices in different curing conditions (Figs. 3 and 4). After the room-temperature curing procedure, the compressive and flexural strengths of the control sample, specimen C, are 106.01 MPa and 12.07 MPa respectively. In the case of high-temperature curing, the compressive and

Table 1
The physicochemical properties of the raw materials.

Compositions	Cement (wt%)	Silica fume (wt%)	Basalt powder (wt%)
CaO	60.65	0.07	9.51
SiO_2	21.21	93.97	47.05
Al_2O_3	8.78	0.03	18.78
Fe_2O_3	4.79	1.78	11.38
MgO	1.57	/	5.42
SO_3	1.12	0.21	1.05
K_2O	1.08	/	1.37
Na_2O	0.80	0.28	2.62
others	1.99	3.62	1.01
Physical properties	Cement	Silica fume	Basalt powder
Density (g/cm^3)	3.15	2.30	2.72
Specific surface area (cm^2/g)	3500	126270	4660

Table 2
The mix proportion of the high-strength cement mortars.

Sample	Binder (100 wt%)			s/b	w/b	SP/b	Slump-flow (mm)
	Cement (wt%)	Basalt powder (wt%)	Silica fume (wt%)				
B	80	20	0	1.0	0.2	1.5%	233
S	80	0	20	1.0	0.2	1.5%	154
C	100	0	0	1.0	0.2	1.5%	252

Note: w/b stands for the water-to-binder ratio, s/b indicates the sand-to-binder ratio, and SP/b represents the superplasticizer-to-binder ratio.

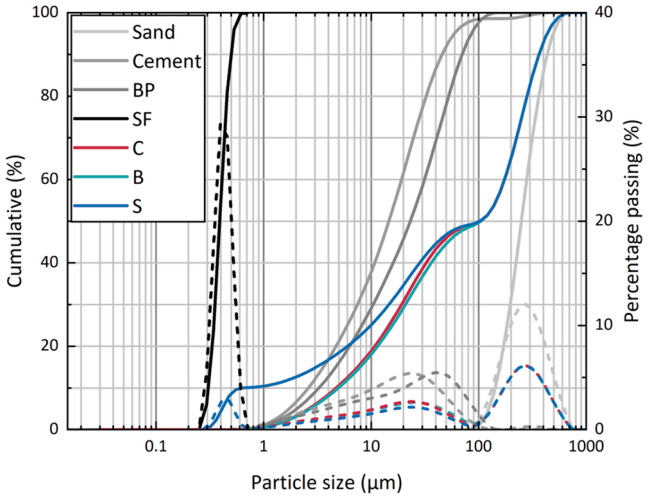

Fig. 2. The particle size distribution of the raw materials; BP indicates basalt powder, and SF denotes silica fume.

flexural strengths of sample C further increase by 11.6% and 16.9% respectively. Compared with the control sample, the replacement of silica fume for cement significantly increases the compressive and flexural strengths of the mortars. Similar findings are also reported regarding the effects of silica fume on the strength of cement matrices [24,25]. The improvement can be attributed to the pozzolanic reaction of silica fume, which causes its filling effect and refines the pore structure of the resultant mortar [30]. After the high-temperature curing procedure, the increase in the compressive strength of the mortars reaches around 11.7%. The increase in the flexural strength of sample S is also about 17.3%.

After the room-temperature curing procedure, the compressive and flexural strengths of sample B, are 97.54 MPa and 11.34 MPa respectively. The high-temperature curing procedure results in the increment of the compressive and flexural strengths of sample B, reaching 19.6% and 25.6% respectively, both of which are higher than those of other samples. It should be noted that adding basalt

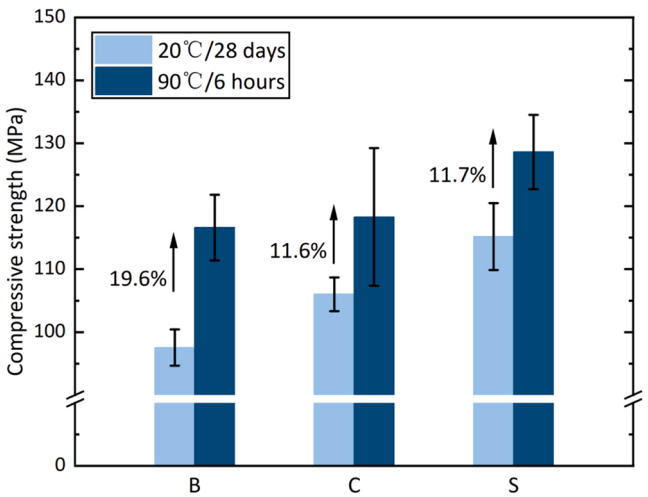

Fig. 3. The compressive strength of the UHSCMs cured by different curing procedures.

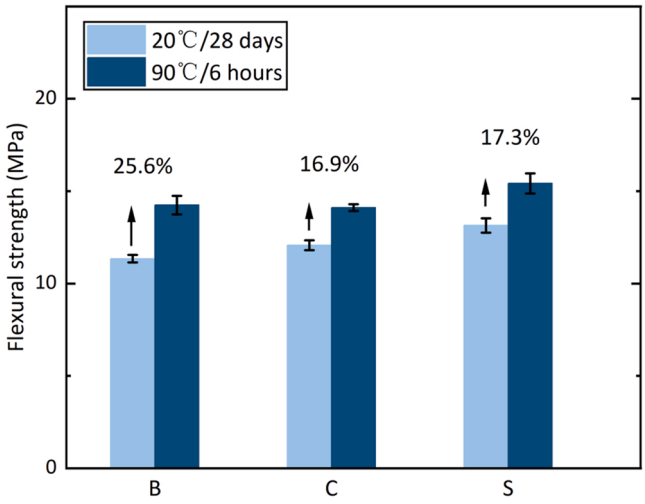

Fig. 4. The flexural strength of the UHSCMs cured by different curing procedures.

powder reduces the compressive and flexural strengths of the cementitious matrix under room-temperature curing conditions. However, the high-temperature curing procedure can enhance the compressive and flexural strengths of sample B to reach that of sample C, possibly because the UHSCMs containing basalt powder may have lower late-age strength [18,31]. The high-temperature curing procedure accelerates the hydration process of the cementitious matrices and eventually leads to the higher strength of the resultant mortar. The above speculation also indicates that the late-age strengths of the UHSCM containing basalt powder (sample B) may be close to those of the control sample. Thus, basalt powder is a potential substance to replace cement in UHSCMs.

3.2. *Pore structures*

Previous literature has reported that the compressive strength of cementitious matrices is associated with their microstructure [32,33]. Fig. 5 delineates the pore size distribution of the prepared UHSCMs, and Fig. 6 illustrates the pore size classification of all samples. Sample S has a lower cumulative pore size distribution (Fig. 5a) than the others, indicating that adding silica fume results in a lower pore volume. Meanwhile, as shown in Fig. 6, most pores belong to gel pores (3.0–4.5 nm) and mesopores (4.5–50.0 nm). The pozzolanic reaction and the filling effect of silica fume are the primary factors leading to the refinement of the pore structure of the UHSCMs containing silica fume [23,28,34]. The refinement of the pore structure of the UHSCMs containing silica fume is one of the reasons for their strength enhancement [35,36].

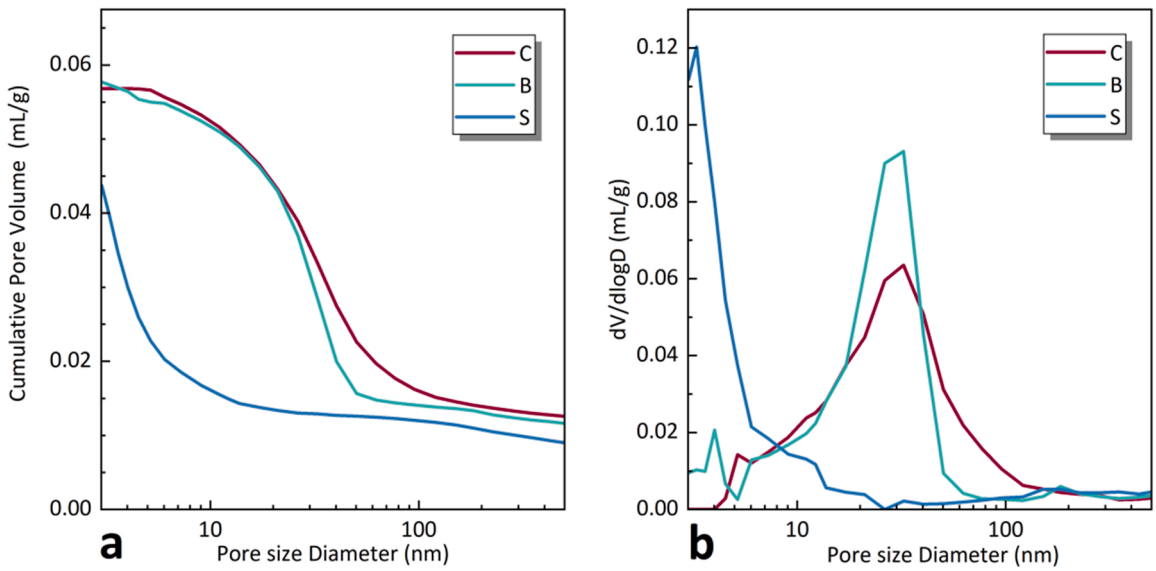

Fig. 5. The (a) cumulative and (b) differential pore size distribution of the UHSCMs.

Samples B and C primarily comprise mesopores, and their total porosities slightly differ. Compared with sample C, adding basalt powder gives rise to the shift of the pore size of the mortars from the medium capillary pore to the mesopore, implying that basalt powder may also refine the pore structure of UHSCMs. Further, according to Fig. 6b, the pore refinement of sample B forms gel pores and increases the pore area. The gel pore volume increases to 2.41 mL/g when basalt powder is added. This pore refinement may be attributed to the pozzolanic reaction of basalt powder. The pozzolanic activity of basalt powder in cementitious matrices is significantly lower [18] than that of silica fume. The relatively lower pozzolanic reactivity of basalt powder may decrease the hydration degree of the UHSCMs, which leads to the relatively lower strengths of sample B compared with the control sample. A close study also reveals that raising the reaction temperature can increase the pozzolanic reactivity of basalt powder [18]. Accordingly, it can explain why higher curing temperatures more dramatically increase the strengths of the UHSCMs containing basalt powder than those of other samples. An increase in the pozzolanic reactivity of basalt powder improves the hydration of the UHSCMs, further refines the pore structure of the mortars, and enhances the strengths of the mortars under high-temperature curing conditions.

3.3. SEM observations

This section focuses on the microstructure of the UHSCMs. The SEM images coupled with the EDXS analysis reveal the microstructure of the prepared UHSCMs. Fig. 7 depicts a hydrated particle of basalt powder found in the cement matrix, and the surface of the particle has a high Mg content, which is seldom found by SEM in cement matrices (see Fig. 7a) due to its tiny content. Thus, element Mg is from basalt powder in sample B. However, it should be noted that the Mg content is also low (5.42%) in basalt powder, as presented in Table 1. The hydration reaction increases the Mg content on the surface of basalt powder particles. In addition, a higher calcium content is observed around basalt powder particles. Calcium enrichment has been reported in the interfacial transition zone (ITZ) between the cement matrix and many types of particles, such as iron particles [37], slag [38], and recycled aggregates [39]. Specifically, Fig. 7b shows a higher Ca content in the ITZ between the cement matrix and sand. Calcium enrichment also occurs in the ITZ between the cement matrix and basalt powder particles, which is beneficial for the pozzolanic reaction of basalt powder and the consumption of $Ca(OH)_2$. However, the SEM images cannot verify the consumption of $Ca(OH)_2$. A high calcium content may form $Ca(OH)_2$ [40]. The following will further analyze the hydration process of basalt powder in UHSCMs using material characterizations.

Comparing the calcium-to-silicon ratios (Ca/Si) in Fig. 7b with those in Fig. 7c reveals that sample S has a lower Ca/Si than the control sample. The Si elements introduced by silica fume lead to the formation of hydration products with a lower Ca/Si in the cement matrix. The hydration products with a lower Ca/Si have more gel pores [41], which is one of the reasons why the gel pores of the UHSCMs containing silica fume are more than those of other samples. In addition, the agglomeration of silica fume is observed in Fig. 7c. Considering that the content of silica fume reaches 20% of the binder, the agglomeration of silica fume appears plausible [24].

Fig. 8 displays the SEM–BSEM image of sample B with the linear elemental distribution determined by EDXS. The red region corresponds to a cross section of basalt powder. Typically, basalt powder is heterogeneous and consists of various minerals. According to the observations in Fig. 7a, it can be assumed that some insoluble minerals may appear on the surface of basalt powder particles after the hydration reaction, leading to a higher Mg content on their surface. Herein, those insoluble minerals may have a higher Mg content. It is also found that the interior structure of basalt powder particles has some pores (the black region). In addition, the Ca/Si of basalt powder is lower than that of the cement matrix. However, the relative calcium content of the basalt powder particles is still higher than what the XRF results present (see Table 1). The following will further analyze the above observations.

3.4. Phase characterizations

The XRD results can be effectively used for crystal phase characterizations. The XRD patterns in Fig. 9 indicate that the existence of olivine in basalt powder enriches the Mg content on the surface of basalt particles [42,43]. Olivine wrapped on the surface of the basalt

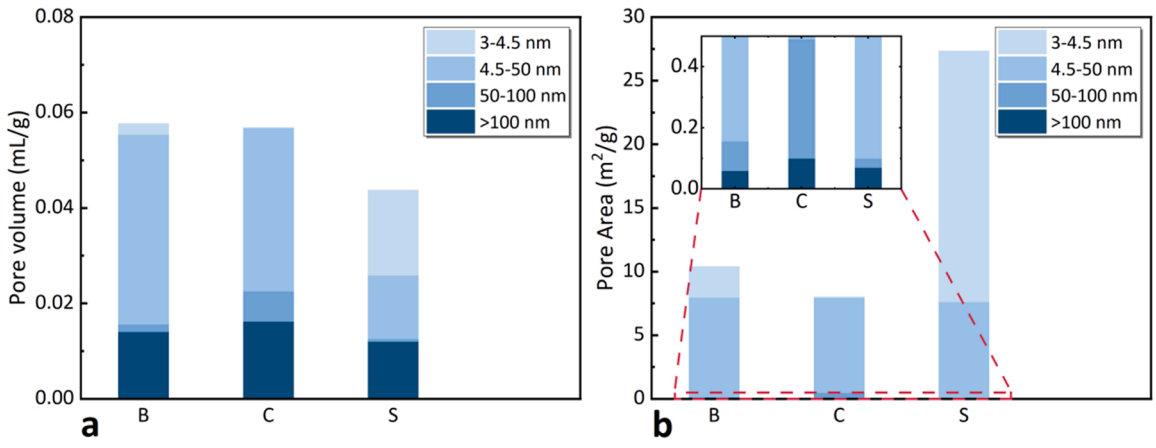

Fig. 6. The pore structure of the UHSCMs: (a) pore volume and (b) pore area.

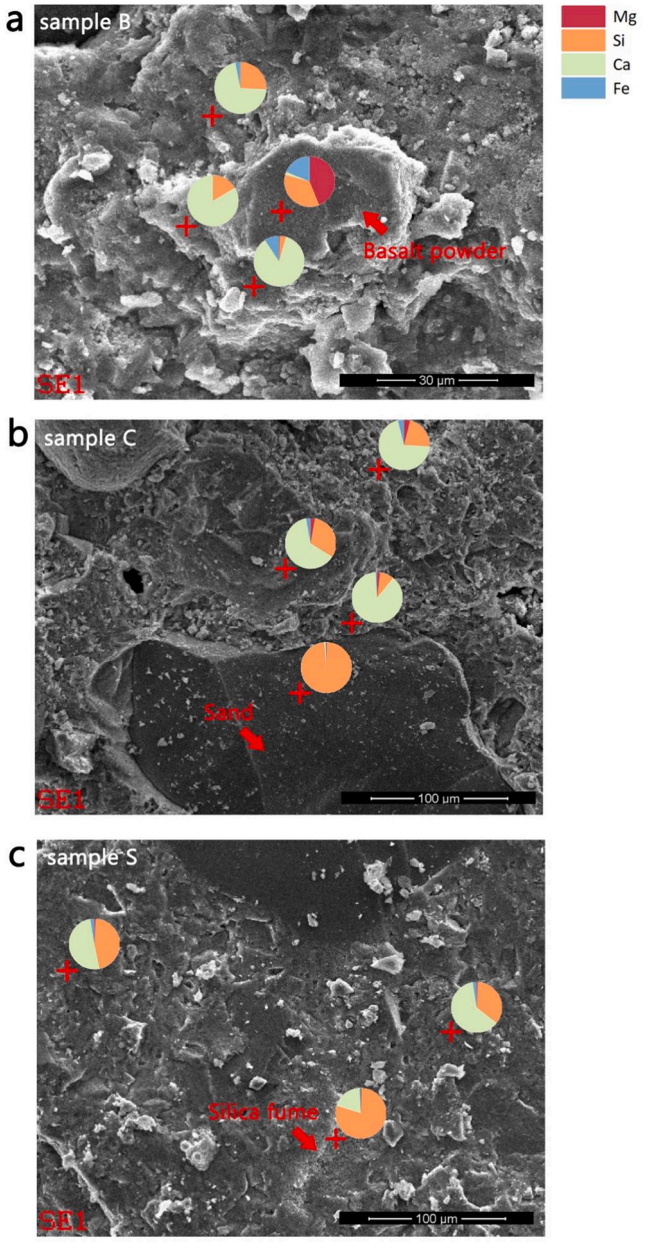

Fig. 7. The SEM images of the samples with the elemental distribution determined by EDXS: (a) basalt powder in sample B; (b) the control sample; (c) sample S.

particles may source from the hydration process. Meanwhile, the XRD results confirm the existence of $Ca(OH)_2$ in samples B and C. According to the established atomic ratios of calcium to silicon in Figs. 7a and 7b, calcium enrichment occurs in the ITZs of basalt powder–cement matrix and sand–cement matrix possibly because $Ca(OH)_2$ forms in the ITZs [44]. Due to the pozzolanic reaction of silica fume, $Ca(OH)_2$ is consumed in sample S [36]. Thus, according to the XRD patterns in Fig. 9 and the FTIR spectra in Fig. 10, there are no characteristic peaks of $Ca(OH)_2$ in sample S [45].

This section concentrates on the effects of basalt powder and silica fume on calcium silicate hydrate (C-S-H) gels. The bands pointing to the Q^2 tetrahedra of C-S-H gels center around 988 cm^{-1} in the FTIR spectra of sample C [45]. In sample B, by adding basalt powder, these bands shift toward a lower frequency (around 1020 cm^{-1}). It is well known that the bands assigned to Si–O stretching vibrations of Q^2 tetrahedra intensify systematically with decreasing Ca/Si [45], which indicates the polymerization of the silicate chain structure in C-S-H gels [45,46]. Hence, adding basalt powder leads to the decrease in Ca/Si and silicate polymerization in UHSCMs.

Further, the appearance of the shoulders at around 1060 cm^{-1} indicates the existence of silica gels in sample S [45,47]. The formation of silica gels is due to the low Ca/Si of the cement matrix containing silica fume [45,48]. As shown in Fig. 7c, the agglomeration

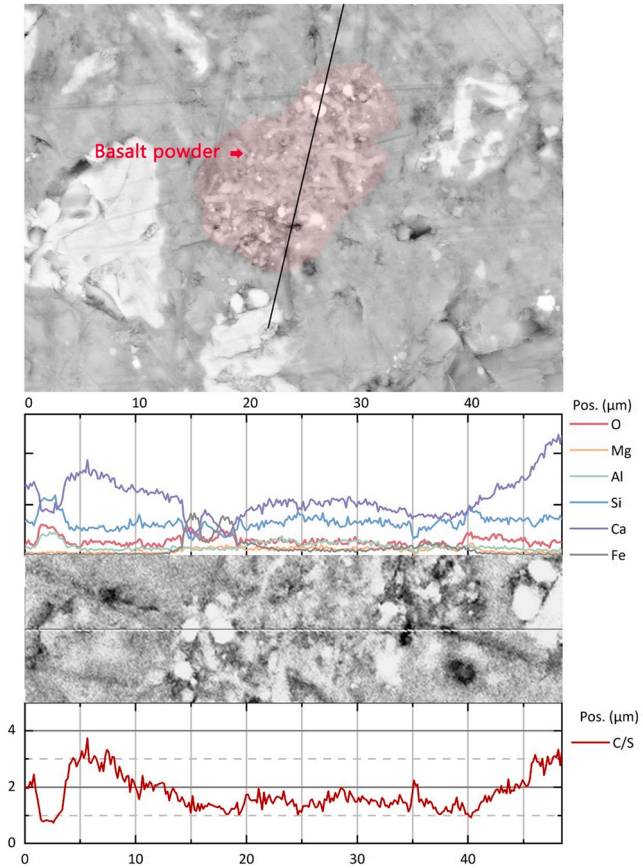

Fig. 8. The SEM–BSEM image of sample B with the linear elemental distribution determined by EDXS.

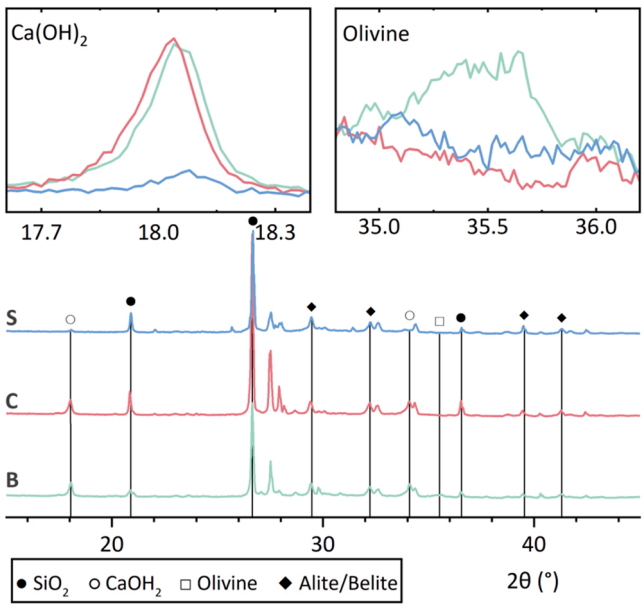

Fig. 9. The XRD patterns of the UHSCMs.

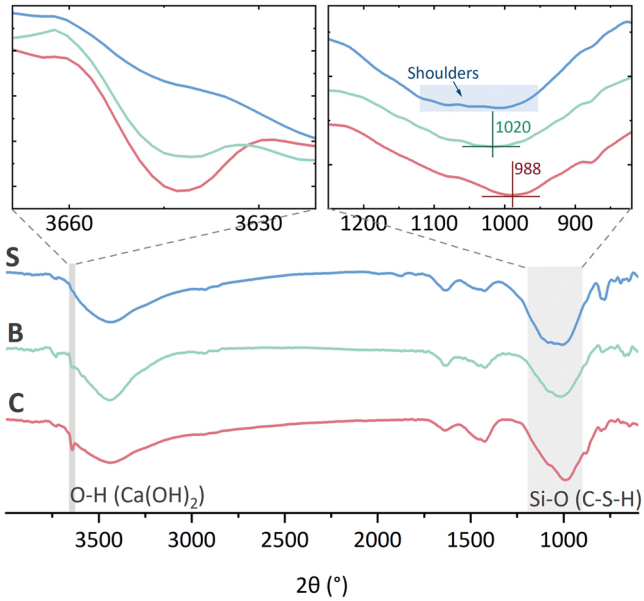

Fig. 10. The FTIR spectra of the UHSCMs.

of silica fume implies that sample S has a low Ca/Si. The FTIR results of all samples demonstrate that basalt powder and silica fume can enhance the degree of silicate polymerization in C-S-H gels [49]. However, the effect of basalt powder is weaker than that of silica fume, which can be explained by its lower pozzolanic reactivity, as discussed in Section 3.2.

Moreover, another difference between basalt powder and silica fume is that basalt powder seldom consumes $Ca(OH)_2$ in UHSCMs. The above finding can be associated with the SEM observation confirming Ca enrichment in the ITZ between the cement matrix and basalt powder particles. $Ca(OH)_2$ is not significantly consumed in the UHSCM containing basalt powder, indicating that the pozzolanic reaction of basalt powder is relatively slight in the cement matrix.

XPS was employed to evaluate the structural changes in C-S-H gels [49]. The binding energy of the Si2p peak of sample B is slightly higher than that of sample S, as depicted in Fig. 11, indicating a higher degree of silicate polymerization in the UHSCM containing basalt powder [50]. It should be noted that there is a slight difference between the Si2p peaks of samples B and S. Meanwhile, the relatively higher binding energies of O1s are associated with a higher proportion of bridging oxygen (BO) and lower Ca/Si [51], which

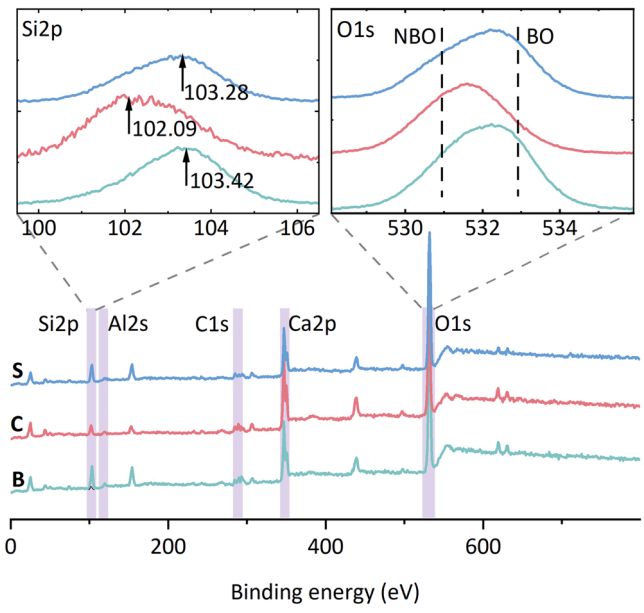

Fig. 11. The XPS results of the UHSCMs.

leads to a higher degree of silicate polymerization. Compared with the control sample, the O1s peak of sample B shifts to higher binding energy, indicating a higher proportion of BO. Sample S also shows a similar trend of O1s spectra, as illustrated in Fig. 11. Thus, the XPS results reveal that both basalt powder and silica fume can improve silicate polymerization in C-S-H gels.

It is well known that silica fume consumes $Ca(OH)_2$ and forms highly polymerized silicate chain structures with a low Ca/Si [52]. However, the effect of basalt powder is not the same as that of silica fume. The effect of silica fume is related to its pozzolanic reactivity in the cement matrix, while the pozzolanic reactivity of basalt powder is low, and it seldom consumes $Ca(OH)_2$. Therefore, the pozzolanic reaction of basalt powder is not the primary reason for the enhancement of silicate polymerization.

The NMR spectra in Fig. 12 illustrate the specific variations of the C-S-H structure of the matrices. Adding silica fume increases the proportion of the Q^2 tetrahedra, indicating a higher degree of silicate polymerization [29]. However, it should be noted that adding basalt powder raises the proportion of the Q^3 and Q^4 tetrahedra, implying the tighter connection of two silicate chains in the C-S-H structures [29]. The above observation can be associated with the decalcification of C-S-H gels [49,53]. Under decalcification conditions, the interlayer calcium of C-S-H gels leaches out, and the linkage of silicate chains increases. Meanwhile, the intensity of the Q^0 peak of sample B is weaker than that of the other samples, indicating that more cement clinker participates in the hydration reaction of the UHSCM with basalt powder. The reduction in the proportion of Q^0 peak is also observed in the decalcified cement pastes [49].

The analysis of the SEM–BSEM image in Fig. 8 demonstrates that the relative calcium content of the hydrated basalt powder is significantly higher than that of the unhydrated basalt powder presented in XRF results. In addition, basalt powder has a loose interior structure. Hence, it is feasible that Ca ions dissolved from the cement clinker may invade basalt powder through pores during the hydration process, in which Ca ions may participate in the hydration reaction inside the basalt powder. The consumption of Ca ions causes the decalcification of the C-S-H gels and the further dissolution of the cement clinker.

Therefore, although both silica fume and basalt powder can enhance the degree of silicate polymerization, their deep-seated mechanisms are different. A higher degree of silicate polymerization forms low-density C-S-H gels [28,54], which agrees with the MIP results of sample S. Low-density C-S-H gels fill the pores and refine the pore structure of the cementitious matrices. The addition of basalt powder to the mortars gives rise to the formation of a double-chain silicate structure [55], which is reported in the decalcification of C-S-H structures and decreases the mechanical properties of calcium silicate hydrate gels [53], leading to the relatively low strengths of sample B (Figs. 3 and 4).

4. Conclusions

This study explores the effect of basalt powder on the hydration process of UHSCMs and provides a basis for applying basalt powder in such cementitious matrices. After the room-temperature curing procedure, the compressive and flexural strengths of UHSCMs containing basalt powder, are 97.54 MPa and 11.34 MPa respectively. Both basalt powder and silica fume can function as reactive additives for UHSCMs and improve silicate polymerization in C-S-H structures. The promotion of silicate polymerization by basalt powder is different from that by silica fume. Silica fume enhances the hydration reaction and silicate polymerization by its pozzolanic reaction, refining the pore structure of the cement matrix. In the UHSCM containing basalt powder, calcium enrichment in the ITZ between the basalt powder particles and the cement matrix leads to the decalcification of C-S-H structures, the formation of a double-chain silicate structure, and the reduction in the UHSCM strengths. Olivine wrapped on the surface of the basalt particles is observed in the cement matrix. The gel pore volume of the UHSCM increases to 2.41 mL/g when basalt powder is added. Finally, a high-temperature curing procedure can alleviate the adverse effects of basalt powder on the strengths of UHSCMs. The high-temperature

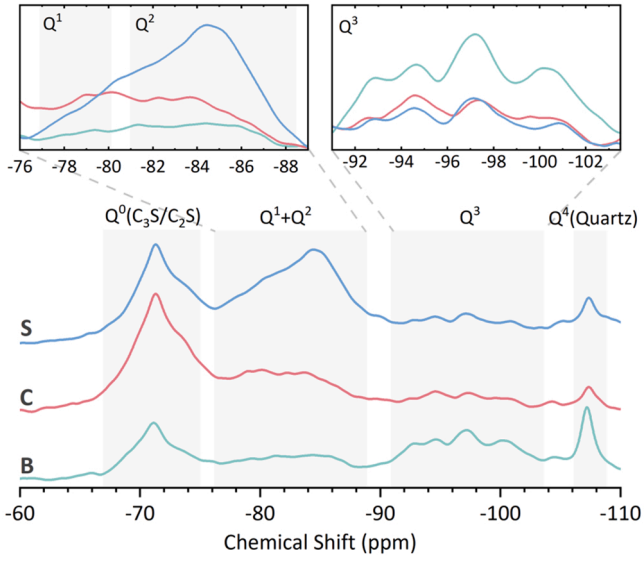

Fig. 12. The NMR results of the UHSCMs.

curing procedure results in the increment of the compressive and flexural strengths of UHSCMs containing basalt powder, reaching 19.6% and 25.6% respectively.

Funding

This work was supported by the Key Deployment Project of the Center for Ocean Mega-Research of Science, Chinese Academy of Science, China (Grant No. COMS2019Q11).

Declaration of Competing Interest

The authors declare that they have no known competing financial interests or personal relationships that could have appeared to influence the work reported in this paper.

Data Availability

Data will be made available on request.

References

[1] N. Farzadnia, A.A. Abang Ali, R. Demirboga, Characterization of high strength mortars with nano alumina at elevated temperatures, Cem. Concr. Res 54 (2013) 43–54, https://doi.org/10.1016/j.cemconres.2013.08.003.
[2] B. Huang, J. Zhu, K. Weng, V.C. Li, J. Dai, Ultra-high-strength engineered/strain-hardening cementitious composites (ECC/SHCC): Material design and effect of fiber hybridization, Cem. Concr. Compos. 129 (2022), 104464, https://doi.org/10.1016/j.cemconcomp.2022.104464.
[3] L. Xu, B. Huang, V.C. Li, J. Dai, High-strength high-ductility Engineered/Strain-Hardening Cementitious Composites (ECC/SHCC) incorporating geopolymer fine aggregates, Cem. Concr. Compos. 125 (2022), 104296, https://doi.org/10.1016/j.cemconcomp.2021.104296.
[4] Z. Wu, C. Shi, K.H. Khayat, Influence of silica fume content on microstructure development and bond to steel fiber in ultra-high strength cement-based materials (UHSC, Cem. Concr. Compos. 71 (2016) 97–109, https://doi.org/10.1016/j.cemconcomp.2016.05.005.
[5] S. Wang, H. Zhu, F. Liu, S. Cheng, B. Wang, L. Yang, Effects of steel fibers and concrete strength on flexural toughness of ultra-high performance concrete with coarse aggregate, Case Stud. Constr. Mater. 17 (2022), e1170, https://doi.org/10.1016/j.cscm.2022.e01170.
[6] A. Said, M. Elsayed, A.A. El-Azim, F. Althoey, B.A. Tayeh, Using ultra-high performance fiber reinforced concrete in improvement shear strength of reinforced concrete beams, Case Stud. Constr. Mater. 16 (2022), e1009, https://doi.org/10.1016/j.cscm.2022.e01009.
[7] J. Lao, L. Xu, B. Huang, J. Dai, S.P. Shah, Strain-hardening Ultra-High-Performance Geopolymer Concrete (UHPGC): Matrix design and effect of steel fibers, Compos. Commun. 30 (2022), 101081, https://doi.org/10.1016/j.coco.2022.101081.
[8] K. Peng, B. Huang, L. Xu, R. Hu, J. Dai, Flexural strengthening of reinforced concrete beams using geopolymer-bonded small-diameter CFRP bars, Eng. Struct. 256 (2022), 113992, https://doi.org/10.1016/j.engstruct.2022.113992.
[9] L. Xu, B. Huang, J. Lao, J. Dai, Tailoring strain-hardening behavior of high-strength Engineered Cementitious Composites (ECC) using hybrid silica sand and artificial geopolymer aggregates, Mater. Des. 220 (2022), 110876, https://doi.org/10.1016/j.matdes.2022.110876.
[10] L. Xu, B. Huang, Q. Lan-Ping, J. Dai, Enhancing long-term tensile performance of Engineered Cementitious Composites (ECC) using sustainable artificial geopolymer aggregates, Cem. Concr. Compos. 133 (2022), 104676, https://doi.org/10.1016/j.cemconcomp.2022.104676.
[11] N. Palankar, A.U. Ravi Shankar, B.M. Mithun, Durability studies on eco-friendly concrete mixes incorporating steel slag as coarse aggregates, J. Clean. Prod. 129 (2016) 437–448, https://doi.org/10.1016/j.jclepro.2016.04.033.
[12] S. Unčík, V. Kmecová, The effect of basalt powder on the properties of cement composites, Procedia Eng. 65 (2013) 51–56, https://doi.org/10.1016/j.proeng.2013.09.010.
[13] M. Dobiszewska, A.K. Schindler, W. Pichór, Mechanical properties and interfacial transition zone microstructure of concrete with waste basalt powder addition, Constr. Build. Mater. 177 (2018) 222–229, https://doi.org/10.1016/j.conbuildmat.2018.05.133.
[14] M. Dobiszewska, R.W. Barnes, Properties of mortar made with basalt powder as sand replacement, Acids Mater. J. 117 (2020) 3–9, https://doi.org/10.14359/51722392.
[15] H. Zhang, T. Ji, H. Liu, S. Su, Modifying recycled aggregate concrete by aggregate surface treatment using sulphoaluminate cement and basalt powder, Constr. Build. Mater. 192 (2018) 526–537, https://doi.org/10.1016/j.conbuildmat.2018.10.160.
[16] H. Binici, Y. Yardim, O. Aksogan, R. Resatoglu, A. Dincer, A. Karrpuz, Durability properties of concretes made with sand and cement size basalt, Sustain. Mater. Technol. 23 (2020), e145, https://doi.org/10.1016/j.susmat.2019.e00145.
[17] G.G.D. Ponzi, V.H.J.M. Santos, R.B. Martel, D. Pontin, A.S.D.G. Stepanha, M.K. Schütz, S.C. Menezes, S.M.O. Einloft, F.D. Vecchia, Basalt powder as a supplementary cementitious material in cement paste for CCS wells: chemical and mechanical resistance of cement formulations for CO_2 geological storage sites, Int J. Greenh. Gas. Control 109 (2021), 103337, https://doi.org/10.1016/j.ijggc.2021.103337.
[18] Y. Li, X. Zeng, J. Zhou, Y. Shi, H.A. Umar, G. Long, Y. Xie, Development of an eco-friendly ultra-high performance concrete based on waste basalt powder for Sichuan-Tibet Railway, J. Clean. Prod. 312 (2021), 127775, https://doi.org/10.1016/j.jclepro.2021.127775.
[19] M. Uysal, Self-compacting concrete incorporating filler additives: Performance at high temperatures, Constr. Build. Mater. 26 (2012) 701–706, https://doi.org/10.1016/j.conbuildmat.2011.06.077.
[20] M. Uysal, K. Yilmaz, Effect of mineral admixtures on properties of self-compacting concrete, Cem. Concr. Compos. 33 (2011) 771–776, https://doi.org/10.1016/j.cemconcomp.2011.04.005.
[21] L. Liu, Y. Zhang, W. Zhang, Z. Liu, L. Zhang, Investigating the influence of basalt as mineral admixture on hydration and microstructure formation mechanism of cement, Constr. Build. Mater. 48 (2013) 434–440, https://doi.org/10.1016/j.conbuildmat.2013.07.021.
[22] A. Mehta, D.K. Ashish, Silica fume and waste glass in cement concrete production: A review, J. Build. Eng. 29 (2020), 100888, https://doi.org/10.1016/j.jobe.2019.100888.
[23] M.J. Shannag, High strength concrete containing natural pozzolan and silica fume, Cem. Concr. Comp. 22 (2000) 399–406, https://doi.org/10.1016/S0958-9465(00)00037-8.
[24] Z. Wu, C. Shi, K.H. Khayat, Influence of silica fume content on microstructure development and bond to steel fiber in ultra-high strength cement-based materials (UHSC, Cem. Concr. Compos. 71 (2016) 97–109, https://doi.org/10.1016/j.cemconcomp.2016.05.005.
[25] Z. Wu, C. Shi, K.H. Khayat, S. Wan, Effects of different nanomaterials on hardening and performance of ultra-high strength concrete (UHSC, Cem. Concr. Compos. 70 (2016) 24–34, https://doi.org/10.1016/j.cemconcomp.2016.03.003.
[26] Chinese National Standard, Test Methods for Flowability of Cement Paste, GB2419–2005, in: China, Beijing, 2005.
[27] Chinese National Standards, Method of Testing Cements - Determination of Strength, GB/T 17671–1999, in: China, Beijing, 1999.
[28] Q. Zeng, K. Li, T. Fen-chong, P. Dangla, Pore structure characterization of cement pastes blended with high-volume fly-ash, Cem. Concr. Res 42 (2012) 194–204.

[29] W. Tian, Y. Liu, W. Wang, Multi-structural evolution of conductive reactive powder concrete manufactured by enhanced ohmic heating curing, Cem. Concr. Compos. 123 (2021), 104199, https://doi.org/10.1016/j.cemconcomp.2021.104199.
[30] H. Vikan, H. Justnes, Rheology of cementitious paste with silica fume or limestone, Cem. Concr. Res. 37 (2007) 1512–1517, https://doi.org/10.1016/j.cemconres.2007.08.012.
[31] J. Kim, Y. Moon, S. Eo, Compressive strength development of concrete with different curing time and temperature, Cem. Concr. Res. 28 (1998) 1761–1773.
[32] H. Reinhardt, M. Stegmaier, Influence of heat curing on the pore structure and compressive strength of self-compacting concrete (SCC), Cem. Concr. Res. 36 (2006) 879–885, https://doi.org/10.1016/j.cemconres.2005.12.004.
[33] J. Jambor, Pore structure and strength development of cement composites, Cem. Concr. Res. 20 (1990) 948–954.
[34] H.A. Toutanji, T. El-Korchi, The influence of silica fume on the compressive strength of cement paste and mortar, Cem. Concr. Res. 25 (1995) 1591–1602, https://doi.org/10.1016/0008-8846(95)00152-3.
[35] M. Oltulu, R. Şahin, Pore structure analysis of hardened cement mortars containing silica fume and different nano-powders, Constr. Build. Mater. 53 (2014) 658–664, https://doi.org/10.1016/j.conbuildmat.2013.11.105.
[36] P. Duan, Z. Shui, W. Chen, C. Shen, Effects of metakaolin, silica fume and slag on pore structure, interfacial transition zone and compressive strength of concrete, Constr. Build. Mater. 44 (2013) 1–6, https://doi.org/10.1016/j.conbuildmat.2013.02.075.
[37] Y. Shen, Q. Li, S. Xu, Microwave absorption properties of cementitious composites containing carbonyl iron powder (CIP) and fly ash: Formation and effect of CIP core–shell structure, Cem. Concr. Compos. 131 (2022), 104559, https://doi.org/10.1016/j.cemconcomp.2022.104559.
[38] J.M. Gao, C.X. Qian, H.F. Liu, B. Wang, L. Li, ITZ microstructure of concrete containing GGBS, Cem. Concr. Res. 35 (2005) 1299–1304, https://doi.org/10.1016/j.cemconres.2004.06.042.
[39] C.S. Poon, Z.H. Shui, L. Lam, Effect of microstructure of ITZ on compressive strength of concrete prepared with recycled aggregates, Constr. Build. Mater. 18 (2004) 461–468, https://doi.org/10.1016/j.conbuildmat.2004.03.005.
[40] K. Garbev, G. Beuchle, M. Bornefeld, L. Black, P. Stemmermann, Cell dimensions and composition of nanocrystalline calcium silicate hydrate solid solutions. Part 1: synchrotron-based X-ray diffraction, J. Am. Ceram. Soc. 91 (2008) 3005–3014, https://doi.org/10.1111/j.1551-2916.2008.02484.x.
[41] S. Igarashi, A. Watanabe, M. Kawamura, Evaluation of capillary pore size characteristics in high-strength concrete at early ages, Cem. Concr. Res 35 (2005) 513–519, https://doi.org/10.1016/j.cemconres.2004.06.036.
[42] D. Świerczyński, C. Courson, L. Bedel, A. Kiennemann, J. Guille, Characterization of Ni−Fe/MgO/Olivine catalyst for fluidized bed steam gasification of biomass, Chem. Mater. 18 (2006) 4025–4032, https://doi.org/10.1021/cm0613511.
[43] P.B. Kelemen, G. Hirth, Reaction-driven cracking during retrograde metamorphism: Olivine hydration and carbonation, Earth Planet Sc. Lett. 345–348 (2012) 81–89, https://doi.org/10.1016/j.epsl.2012.06.018.
[44] W. Ding, W. Xu, P. Dong, Y. Liu, T. Shiotani, Roles of CSH gel in the microstructure and piezoelectric properties variation of cement-based piezoelectric ceramic composite, Mater. Lett. 306 (2022), 130952.
[45] P. Yu, R.J. Kirkpatrick, B. Poe, P.F. McMillan, X. Cong, Structure of calcium silicate hydrate (C-S-H): near-, mid-, and far-infrared spectroscopy, J. Am. Ceram. Soc. 82 (1999) 742–748, https://doi.org/10.1111/j.1151-2916.1999.tb01826.x.
[46] S. Xu, Y. Shen, Q. Li, X. Liu, Hybrid effects of polyvinyl alcohol (PVA) and basalt fibers on microwave absorption of cement composites with fly ash, J. Am. Ceram. Soc. (2021), https://doi.org/10.1111/jace.17992.
[47] V. Lilkov, E. Dimitrova, O.E. Petrov, Hydration process of cement containing fly ash and silica fume: The first 24 h, Cem. Concr. Res. 27 (1997) 577–588, https://doi.org/10.1016/S0008-8846(97)00025-2.
[48] L. Li, D. Xuan, S.H. Chu, C.S. Poon, Modification of recycled aggregate by spraying colloidal nano silica and silica fume, Mater. Struct. 54 (2021) 1–15.
[49] K. Kurumisawa, T. Nawa, H. Owada, M. Shibata, Deteriorated hardened cement paste structure analyzed by XPS and 29Si NMR techniques, Cem. Concr. Res 52 (2013) 190–195, https://doi.org/10.1016/j.cemconres.2013.07.003.
[50] L. Black, K. Garbev, I. Gee, Surface carbonation of synthetic C-S-H samples: a comparison between fresh and aged C-S-H using X-ray photoelectron spectroscopy, Cem. Concr. Res. 38 (2008) 745–750, https://doi.org/10.1016/j.cemconres.2008.02.003.
[51] L. Black, K. Garbev, P. Stemmermann, K.R. Hallam, G.C. Allen, Characterisation of crystalline C-S-H phases by X-ray photoelectron spectroscopy, Cem. Concr. Res 33 (2003) 899–911, https://doi.org/10.1016/S0008-8846(02)01089-X.
[52] Z. Wu, J.F. Young, The hydration of tricalcium silicate in the presence of colloidal silica, J. Mater. Sci. 19 (1984) 3477–3486, https://doi.org/10.1007/BF00552262.
[53] L. Liu, C. Sun, G. Geng, P. Feng, J. Li, R. Dähn, Influence of decalcification on structural and mechanical properties of synthetic calcium silicate hydrate (C-S-H), Cem. Concr. Res. 123 (2019), 105793, https://doi.org/10.1016/j.cemconres.2019.105793.
[54] Y. Shen, Q. Li, S. Xu, X. Liu, Electromagnetic wave absorption of multifunctional cementitious composites incorporating polyvinyl alcohol (PVA) fibers and fly ash: Effects of microstructure and hydration, Cem. Concr. Res. 143 (2021), 106389, https://doi.org/10.1016/j.cemconres.2021.106389.
[55] F. Matsushita, Y. Aono, S. Shibata, Calcium silicate structure and carbonation shrinkage of a tobermorite-based material, Cem. Concr. Res. 34 (2004) 1251–1257, https://doi.org/10.1016/j.cemconres.2003.12.016.